

Contents lists available at [SciVerse ScienceDirect](http://SciVerse.ScienceDirect.com)

NeuroImage

journal homepage: [www.elsevier.com/locate/ynimg](http://www.elsevier.com/locate/ynimg)

## Discriminative analysis of early Alzheimer's disease using multi-modal imaging and multi-level characterization with multi-classifier (M3)

Zhengjia Dai<sup>a,1</sup>, Chaogan Yan<sup>a,1</sup>, Zhiqun Wang<sup>b</sup>, Jinhui Wang<sup>a</sup>, Mingrui Xia<sup>a</sup>, Kuncheng Li<sup>b,c</sup>, Yong He<sup>a,\*</sup>

<sup>a</sup> State Key laboratory of Cognitive Neuroscience and Learning, Beijing Normal University, Beijing, 100875, China

<sup>b</sup> Department of Radiology, Xuanwu Hospital of Capital Medical University, Beijing, China

<sup>c</sup> Key Laboratory for Neurodegenerative Diseases (Capital Medical University), Ministry of Education, China

### ARTICLE INFO

#### Article history:

Received 5 August 2011

Revised 27 September 2011

Accepted 3 October 2011

Available online xxx

#### Keywords:

Alzheimer's disease

MRI

fMRI

ALFF

ReHo

Connectivity

Network

Connectome

### ABSTRACT

Increasing attention has recently been directed to the applications of pattern recognition and brain imaging techniques in the effective and accurate diagnosis of Alzheimer's disease (AD). However, most of the existing research focuses on the use of single-modal (e.g., structural or functional MRI) or single-level (e.g., brain local or connectivity metrics) biomarkers for the diagnosis of AD. In this study, we propose a methodological framework, called multi-modal imaging and multi-level characteristics with multi-classifier (M3), to discriminate patients with AD from healthy controls. This approach involved data analysis from two imaging modalities: structural MRI, which was used to measure regional gray matter volume, and resting-state functional MRI, which was used to measure three different levels of functional characteristics, including the amplitude of low-frequency fluctuations (ALFF), regional homogeneity (ReHo) and regional functional connectivity strength (RFCS). For each metric, we computed the values of ninety regions of interest derived from a prior atlas, which were then further trained using a multi-classifier based on four maximum uncertainty linear discriminant analysis base classifiers. The performance of this method was evaluated using leave-one-out cross-validation. Applying the M3 approach to the dataset containing 16 AD patients and 22 healthy controls led to a classification accuracy of 89.47% with a sensitivity of 87.50% and a specificity of 90.91%. Further analysis revealed that the most discriminative features for classification are predominantly involved in several default-mode (medial frontal gyrus, posterior cingulate gyrus, hippocampus and parahippocampal gyrus), occipital (fusiform gyrus, inferior and middle occipital gyrus) and subcortical (amygdale and pallidum of lenticular nucleus) regions. Thus, the M3 method shows promising classification performance by incorporating information from different imaging modalities and different functional properties, and it has the potential to improve the clinical diagnosis and treatment evaluation of AD.

© 2011 Elsevier Inc. All rights reserved.

### Introduction

Alzheimer's disease (AD), which is the most common form of dementia, is a progressive neurodegenerative disease that is clinically characterized by the decline in memory and other cognitive functions. It gradually destroys patients' memories and abilities to reason, make judgments, communicate and deal with daily activities (Jeong, 2004). Since the mid-1980s, the prevalence rate of dementia in persons aged 65 years or greater has been reported to be 3.6–10.3% in Western countries and 1.8–10.8% in Asian countries (Lee et al., 2002). Approximately 50–60% of patients with dementia are estimated to have AD. To improve the level of both basic AD research and clinical intervention for patients with AD, it is crucial to find a valid and objective biomarker to distinguish patients with early-stage AD from healthy controls (Chapman et al., 2007).

Machine learning and pattern classification techniques have played an important role in exploring the brain differences between patients with AD and healthy controls. Many studies have demonstrated that these techniques, in combination with structural and functional neuroimaging data, are useful for finding potential biomarkers for AD. For example, several brain imaging methods including electroencephalography (EEG) and positron emission tomography (PET) have been used to study the diagnosis of AD (Bennys et al., 2001; Besthorn et al., 1997; Kippenhan et al., 1994; Lehmann et al., 2007; Minoshima et al., 1995). More recently, some studies have employed structural MRI data to investigate automatic classification methods of AD according to extracted features such as vertex-based cortical thickness (Desikan et al., 2009; Lerch et al., 2008) and voxel-wise volume characteristics (Davatzikos et al., 2008a, 2008b; Fan et al., 2007; Klöppel et al., 2008; Lao et al., 2004; Magnin et al., 2008). Using resting-state functional MRI (R-fMRI) data, several research groups have proposed regional or connectivity metrics such as the cross-correlations of spontaneous low frequency (Li et al., 2002), goodness-of-fit analysis of the default mode network (Greicius et al., 2004), intrinsically anti-correlated networks

\* Corresponding author.

E-mail address: [yong.he@bnu.edu.cn](mailto:yong.he@bnu.edu.cn) (Y. He).

<sup>1</sup> These authors contributed equally to this work.

(Wang et al., 2006) and whole-brain connectivity matrices (Chen et al., 2011) as classification features of AD.

Despite these advances, previous discriminative studies of AD mainly focus on a single modality of biomarkers, which might capture partial information about brain abnormalities and therefore influence the resulting classification performance. Several recent studies have demonstrated that multi-modal imaging using integrative information was able to significantly improve the discrimination accuracy of the AD diagnosis (Apostolova et al., 2010; Fan et al., 2007; Walhovd et al., 2010; Zhang et al., 2011). These studies mainly combine MRI, PET, cerebral blood flow (CBF) and cerebrospinal fluid (CSF) techniques. To date, very few studies have used a combination of structural MRI and R-fMRI data to discriminate patients with AD from healthy controls. Structural MRI data contains rich morphological information about brain tissues and has been widely used to study gray matter atrophy in AD (Baron et al., 2001; Chetelat and Baron, 2003; Hirata et al., 2005; Karas et al., 2003). R-fMRI is a promising non-invasive imaging technique used to measure spontaneous brain activity in vivo and is crucial for the understanding of intrinsic brain functional architecture under both normal and pathological conditions (Biswal et al., 1995, 2010; Fox and Greicius, 2010; Fox and Raichle, 2007; Wang et al., 2010; Zhang and Raichle, 2010). Several studies have used R-fMRI to demonstrate that AD is associated with changes in functional characteristics at different levels, including the amplitude of low-frequency fluctuations (ALFF) (Wang et al., 2011), intra-regional synchronization (He et al., 2007) and inter-regional functional connectivity (Allen et al., 2007; Greicius et al., 2004; Li et al., 2002; Supekar et al., 2008; Wang et al., 2007).

In this study, we propose a methodological framework, multi-modal imaging (structural and functional MRI) and multi-level characteristics [ALFF, regional homogeneity (ReHo) and regional functional connectivity strength (RFCS) for R-fMRI] with multi-classifier (M3), to discriminate AD patients from healthy controls. By effectively integrating enriched and comprehensive information, this approach could improve the classification power compared to previously used techniques. The rest of this paper is organized as follows: we first introduce our experimental data acquisition, feature extraction, discriminative analysis and identification of the most discriminative features in the **Materials and methods** section and then present the main experimental results in the **Results** section and relevant discussion in the **Discussion** section.

## Materials and methods

### Subjects

Twenty-four healthy controls and nineteen early AD patients participated in this study. All subjects were right-handed native Chinese speakers. Written informed consent was obtained from all subjects before they participated in the study. All of the AD patients were recruited from a memory outpatient clinic at Xuanwu Hospital, Beijing, China. The healthy controls were recruited by advertisement from the local community. This study was approved by the Medical Research Ethics Committee of Xuanwu Hospital. The diagnosis criteria for AD fulfilled the Diagnostic and Statistic Manual Disorders, Fourth Edition (American Psychiatric Association, 1994) criteria for dementia, and the National Institute of Neurological and Communicative Disorders and Stroke/Alzheimer Disease and Related Disorders Association (NINCDS-ADRDA) (McKhann et al., 1984) criteria for AD. The subjects were assessed clinically with the Clinical Dementia Rating (CDR) score (Morris, 1993) as healthy controls (CDR = 0) or as patients with early stages of AD (7 patients with CDR = 1 and 12 patients with CDR = 0.5). All AD patients underwent complete physical and neurological examination, an extensive battery of neuropsychological assessments and standard laboratory tests. All healthy controls had no history of neurological or psychiatric disorders, sensorimotor impairment or cognitive complaints, and no abnormal findings were identified by

conventional brain MRI. We discarded the data of two healthy controls and three AD patients due to excessive motion (see **Data preprocessing**). Clinical and demographic data for the remaining 38 participants are shown in **Table 1**. The data have previously been used to detect brain regional abnormalities in AD (Wang et al., 2011).

### Data acquisition

All subjects were scanned on a Siemens 3 Tesla Magnetom Sonata scanner (Siemens, Erlangen, Germany). Foam padding and headphones were used to limit head movement and reduce scanner noise. During data acquisition, the subjects were instructed to keep their eyes closed but not fall asleep, to relax their minds, and to move as little as possible. Functional images were collected axially using an echo-planar imaging (EPI) sequence. The imaging parameters are as follows: repetition time (TR)/echo time (TE) = 2000 ms/40 ms; flip angle (FA) = 90°; field of view (FOV) = 24 cm; matrix = 64 × 64; slices = 28; thickness = 4 mm; voxel size = 3.75 × 3.75 × 4 mm<sup>3</sup>; gap = 1 mm; and bandwidth = 2232 Hz/pixel. The scan lasted for 478 s. Three dimensional T1-weighted magnetization-prepared rapid gradient echo (MPRAGE) sagittal images were collected using the following parameters: TR/TE = 1900 ms/2.2 ms; FA = 9°; inversion time (TI) = 900 ms; matrix = 256 × 256; slices = 176; thickness = 1.0 mm; and voxel size = 1 × 1 mm<sup>3</sup>.

### Feature extraction

#### Functional MRI data

**Data preprocessing.** Unless otherwise stated, all functional imaging data preprocessing was carried out using Statistical Parametric Mapping (SPM5, <http://www.fil.ion.ucl.ac.uk/spm>) and Data Processing Assistant for Resting-State fMRI (DPARSF) (Yan and Zang, 2010). Because of the instability of the initial signal and participants' adaptation to the scanning, the first 10 functional images were discarded. The remaining fMRI images were first corrected for within-scan acquisition time differences between slices and further realigned to the first volume to correct for interscan head motions. Five subjects (2 AD patients with CDR = 1, 1 AD patient with CDR = 0.5 and 2 healthy controls) were excluded from further analysis because of their excessive movement (>2 mm or 2°). The motion-corrected functional volumes were then spatially normalized onto stereotaxic space (Talairach and Tournoux, 1988) using an optimum 12-parameter affine transformation and nonlinear deformation (Ashburner and Friston, 2005) and then resampled to 3 mm isotropic voxels. Next, temporal band-pass filtering (0.01 Hz–0.1 Hz) was performed on the time series of each voxel using the Resting-State fMRI Data Analysis Toolkit (REST, <http://rest.restfmri.net>) (Song et al., 2011) to reduce the effect of low-frequency drifts and high-frequency physiological noise (Biswal et al., 1995; Lowe et al., 1998). We then calculated ALFF, ReHo and RCS as described below.

**Table 1**  
Characteristics of AD patients and normal controls.

Characteristics	AD	Controls	P value
N (M/F)	16 (8/8)	22 (7/15)	0.26 <sup>a</sup>
Age, years	69.56 ± 7.65	66.55 ± 7.67	0.09 <sup>b</sup>
Education, years	10.06 ± 3.39	10.00 ± 3.93	0.96 <sup>b</sup>
MMSE	18.50 ± 3.24	28.59 ± 0.59	<0.0001 <sup>b</sup>

MMSE, Mini-Mental State Examination; plus-minus values are means ± S.D.

<sup>a</sup> The P value for gender distribution in the two groups was obtained by Chi-square test.

<sup>b</sup> The P values were obtained by a two-sample two-tailed t-test.

**ALFF analyses.** We used REST software to calculate the ALFF. ALFF is physiologically meaningful for measuring regional intrinsic or spontaneous neuronal activity of the brain (Zang et al., 2007). Briefly, for a given voxel, the time series was first converted to the frequency domain using a Fast Fourier Transform. The square root of the power spectrum was computed and then averaged across 0.01–0.1 Hz. This averaged square root was taken as the ALFF (Zang et al., 2007). To reduce the global effects of variability across participants, as used in many PET studies, the ALFF of each voxel was divided by the global mean ALFF value for each subject. The individual ALFF maps were then partitioned into 90 regions of interest (ROIs) in terms of the Automated Anatomical Labeling (AAL) atlas (45 for each hemisphere, see Table 2) (Tzourio-Mazoyer, 2002), and the mean ALFF value of each region was acquired by averaging the ALFF values within that region.

**ReHo analyses.** We used REST software to calculate the ReHo. The ReHo method (Zang et al., 2004) was originally proposed to measure the degree of regional synchronization of fMRI time courses. ReHo was defined as the Kendall's coefficient of concordance (KCC) (Kendall and Gibbons, 1990) of the time series of a given voxel with those of its nearest neighbors. A larger ReHo value for a given voxel indicates a higher regional coherence. The number of neighboring voxels was set as 26. To reduce the global effects of variability across participants, as used in ALFF analyses, the ReHo of each voxel was divided by the global mean ReHo value for each subject. The individual ReHo maps were then partitioned into 90 ROIs using the AAL atlas, and the mean ReHo value of each region was acquired by averaging the ReHo values within that region.

**Regional Functional Correlation Strength (RFCS) analyses.** To compute resting-state function connectivity, we regressed out several spurious effects of nuisance covariates (Fox et al., 2005): (1) six parameters obtained by head motion correction, three for translation and three for rotation and (2) whole brain signal averaged over entire brain. The individual volume was first partitioned into 90 ROIs using the AAL atlas, and the mean time series of each region was then extracted by averaging the time series within that region. To measure the functional connectivity among regions, we calculated the Pearson correlation coefficients between all possible pairs of regions. We obtained a  $90 \times 90$  correlation matrix for each subject. We then measured RFCS

using a method that has been described in previous studies (He et al., 2009; Jiang et al., 2004). The correlation strength of region  $i$  was defined as:

$$S_{region}(i) = \frac{1}{N-1} \sum_{j \neq i} |R_{ij}| \quad (1)$$

where  $R_{ij}$  is the correlation coefficient between region  $i$  and region  $j$ , and  $N$  is the number of regions. RFCS measures the average correlation extent of a given region with all of the other regions.

#### Structural MRI data

Individual structural images (T1-weighted MPRAGE images) were coregistered to the mean functional image after motion correction using a linear transformation (Collignon et al., 1995). The transformed structural images were then segmented into gray matter density (GMD), white matter density (WMD) and cerebrospinal fluid density and spatially normalized into standard space using a unified segmentation algorithm (Ashburner and Friston, 2005). Individual GMD images underwent spatial smoothing using 10-mm full width at half maximum (FWHM) Gaussian kernel and then resampled to 3 mm isotropic voxels. Like functional maps, individual GMD maps were first partitioned into 90 ROIs using the AAL atlas, and the mean GMD value of each region was then extracted by averaging the GMD values of all voxels within that region.

We obtained three functional maps at different levels, i.e., the ALFF map, ReHo map, RFCS map, and one structural map, the GMD map, for each subject. For each map, 90 features were extracted from the 90 ROIs. For a given ROI, ALFF, ReHo and RFCS reflect the degree of regional activity, the degree of regional synchronization and the degree of global synchronization of spontaneous neuronal activity, respectively. The GMD captures the morphometric characteristics of the given ROIs. Therefore, we extracted 90 features separately from the ALFF, ReHo, RFCS and GMD maps for each subject. It is worth noting that the features derived from other modalities and levels can also be used as additional features for classification.

#### Discriminative analysis

In this section, we first detail the main procedures of classifying AD patients MRI and healthy controls. The procedures included three

**Table 2**  
Regions of interest (ROIs) included in AAL-atlas.

Regions	Abbreviations	Regions	Abbreviations
Superior frontal gyrus, dorsolateral	SFGdor	Middle frontal gyrus, orbital part	ORBmid
Middle frontal gyrus	MFG	Inferior frontal gyrus, orbital part	ORBinf
Inferior frontal gyrus, opercular part	IFGoperc	Superior frontal gyrus, medial orbital	ORBsupmed
Inferior frontal gyrus, triangular part	IFGtriang	Gyrus rectus	REC
Rolandic operculum	ROL	Insula	INS
Supplementary motor area	SMA	Anterior cingulate and paracingulate gyri	ACG
Superior frontal gyrus, medial	SFGmed	Median cingulate and paracingulate gyri	DCG
Cuneus	CUN	Posterior cingulate gyrus	PCG
Lingual gyrus	LING	Parahippocampal gyrus	PHG
Superior occipital gyrus	SOG	Temporal pole: superior temporal gyrus	TPOsup
Middle occipital gyrus	MOG	Temporal pole: middle temporal gyrus	TPOmld
Inferior occipital gyrus	IOG	Olfactory cortex	OLF
Fusiform gyrus	FFG	Hippocampus	HIP
Superior parietal gyrus	SPG	Amygdala	AMYG
Inferior parietal, but supramarginal and angular gyri	IPL	Caudate nucleus	CAU
Supramarginal gyrus	SMG	Lenticular nucleus, putamen	PUT
Angular gyrus	ANG	Lenticular nucleus, pallidum	PAL
Precuneus	PCUN	Thalamus	THA
Paracentral lobule	PCL	Precentral gyrus	PreCG
Superior temporal gyrus	STG	Calcarine fissure and surrounding cortex	CAL
Middle temporal gyrus	MTG	Postcentral gyrus	PoCG
Inferior temporal gyrus	ITG	Heschl gyrus	HES
Superior frontal gyrus, orbital part	ORBsup		

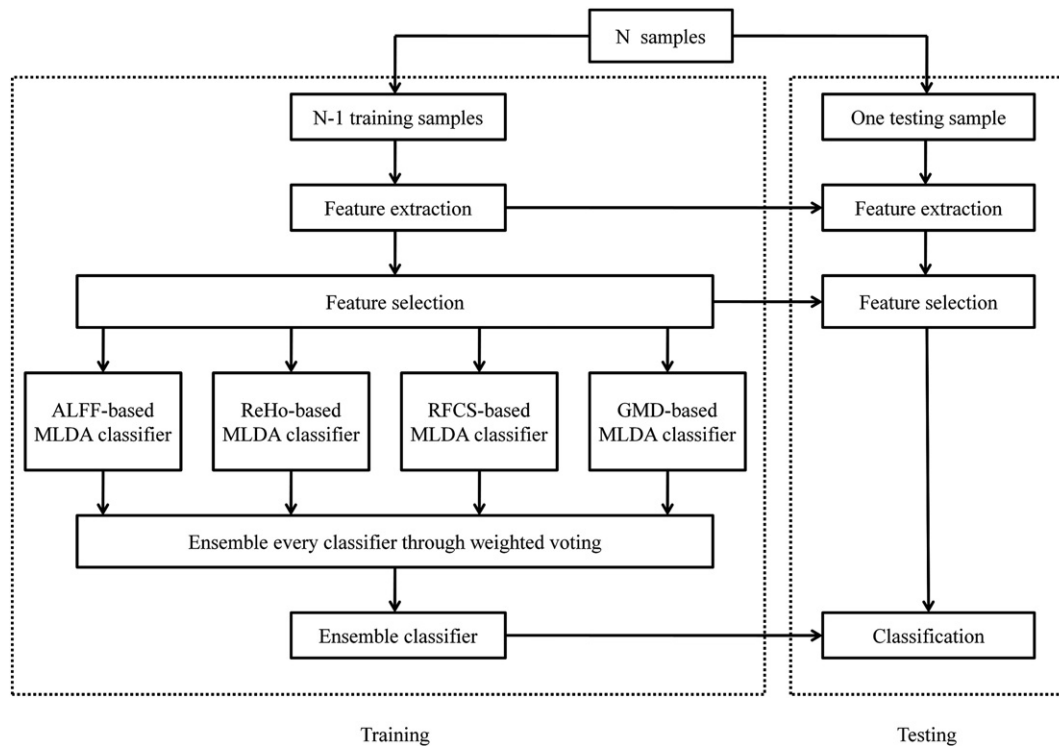


Fig. 1. A flowchart of the M3 method used for classification.

steps: feature selection, maximum uncertainty linear discriminant analysis (MLDA)-based classification and multi-classifier, as shown in Fig. 1. Leave-one-out cross-validation (LOOCV) was then used to estimate the performance of our classifier. Finally, we identified the most discriminative features.

#### Feature selection

Given that some features are less effective, irrelevant or redundant for classification, selecting a small set of features with the greatest discriminative power will improve the final classification performance (Dosenbach et al., 2010; Guyon, 2003). Several studies have suggested that correctly reducing the number of features can not only speed up computation but also improve the performance of the classifier (De Martino et al., 2008; Pereira et al., 2009). Therefore, a univariate feature-filtering step was adopted in this study. Two-sample two-tailed t-tests were performed to determine the features that showed differences between the AD and NC groups. We also used a nonparametric rank-sum test for the feature selection and found similar results (data not shown). This process was constrained on the training set of each LOOCV fold. Features with significant differences ( $P < 0.05$ , uncorrected) between the two groups of training set were selected. The feature selection was always carried out on the training sample only, which avoided the overfitting of the classifier.

#### MLDA-based classifier

We used MLDA as our base classifier. The primary purpose of Fisher Discriminant Analysis (FDA) was to find the optimal projective direction by maximizing between-class separability and minimizing within-class variability. When the high-dimensional space samples are mapped onto one dimension, we can easily perform classification using one-dimensional projected features. However, the traditional FDA cannot be directly used when the within-class scatter matrix is singular, as is the case of limited samples and high dimensional feature space. In this work, the dimension of feature space was still higher than the number of samples even after performing feature selection. Thus, we used a maximum uncertainty LDA-based approach (MLDA)

(Thomaz et al., 2004, 2007). This method employed a maximum entropy covariance selection method instead of the within-class scatter matrix.

#### Multi-classifier

Many researchers have investigated the technique of combining the predicted results of multiple classifiers to generate a single classifier (Hong et al., 1999; Kittler et al., 1998; Ross and Jain, 2003). A multi-classifier was used in this study. Fig. 1 illustrates the basic framework for the multi-classifier. Briefly, one subject was first selected as a test sample, and the remaining subjects were used to build a multi-classifier. We applied four different types of features (ALFF, ReHo, RFCS and GMD) to obtain the base classifier. The four classifiers were combined through weighted voting. As an example, if we had  $n$  subjects, one was selected for testing, and the remaining  $n-1$  subjects were used for training the base classifier's parameter values. From

Table 3

Classification performance of the single metrics and multi-modal multi-level combinations.

Metrics	Accuracy	Sensitivity	Specificity
The proposed M3 method (ALFF + ReHo + RFCS + GMD)	89.47%	87.5%	90.91%
ALFF	78.95%	81.25%	77.27%
ReHo	73.68%	75%	72.73%
RFCS	73.68%	81.25%	68.18%
GMD	86.84%	87.5%	86.36%
ALFF + ReHo	76.32%	68.75%	81.82%
ALFF + RFCS	73.68%	75%	72.73%
ReHo + RFCS	68.42%	75%	63.64%
GMD + ALFF	86.84%	87.5%	86.36%
GMD + ReHo	86.84%	87.5%	86.36%
GMD + RFCS	86.84%	87.5%	86.36%
ALFF + ReHo + RFCS	76.32%	75%	77.27%
GMD + ALFF + ReHo	81.58%	81.25%	81.82%
GMD + ALFF + RFCS	86.84%	81.25%	90.91%
GMD + ReHo + RFCS	86.84%	87.5%	86.36%

**Table 4**  
The number of features retained in the M3 method per fold.

Fold	ALFF	ReHo	RFCS	GMD
1	11	17	7	88
2	9	12	6	88
3	11	18	10	89
4	10	17	9	89
5	12	17	8	88
6	9	15	7	89
7	11	14	7	88
8	10	14	8	88
9	11	17	8	88
10	10	18	9	89
11	11	20	10	89
12	11	16	6	88
13	11	15	7	86
14	10	15	6	86
15	11	15	6	87
16	10	16	6	89
17	10	16	10	88
18	10	16	6	88
19	10	20	8	89
20	11	13	6	89
21	12	16	6	88
22	10	17	10	88
23	11	14	6	88
24	11	18	6	88
25	11	15	6	88
26	10	16	8	89
27	11	18	9	88
28	10	16	6	88
29	11	14	6	88
30	12	15	7	89
31	10	16	6	88
32	10	15	5	89
33	12	18	7	88
34	12	16	6	88
35	12	20	10	88
36	11	17	6	88
37	11	16	6	88
38	13	15	7	88

these  $n-1$  training samples, we can obtain each base classifier's weight of voting by calculating its classification accuracy of  $n-1$  leave-one-out within the training set. The multi-classifier was then determined by the weighted sum of each base classifier's output label:

$$F(x_i) = \text{sign} \left( \sum_{k=1}^4 (\omega_k \cdot F_k(x_i^k)) \right) \quad (2)$$

where  $x_i = \{x_i^k, k = 1, 2, 3, 4\}$  a feature vector of the four feature map of  $i$ -th test sample,  $x_i^k$  is a feature vector of the  $k$ -th feature map,  $F_k \in \{-1, 1\}$  as its corresponding classifier's output, and  $\omega_k$  is  $k$ -th classifier's weight of voting obtained by the classification accuracy of  $n-1$  leave-one-out within the training set.

**Cross validation**

LOOCV was used to estimate the performance of classifier. In LOOCV, each sample was designated as the test sample, while the remaining samples were used to train the multi-classifier. Accuracy, sensitivity and specificity can be defined on the basis of prediction results of LOOCV to quantify the performance of the classifier.

$$\text{Accuracy} = \frac{TP + TN}{TP + FN + TN + FP} \quad (3)$$

$$\text{Sensitivity} = \frac{TP}{TP + FN} \quad (4)$$

$$\text{Specificity} = \frac{TN}{TN + FP} \quad (5)$$

where TP, FN, TN, and FP denoted the number of patients correctly predicted, the number of patients classified as normal controls, the number of normal controls correctly predicted and the number of normal controls classified as patients, respectively.

**Identification of the most discriminative features**

For each base classifier, the classification rule is based on the determination of the separating hyperplane, which is orthogonal to the discrimination hyperplane or projective direction. It has been shown that the coefficients of the discrimination hyperplane quantify the amount of discriminative feature information (Mourão-Miranda et al., 2005; Sato et al., 2009; Thomaz et al., 2004; Thomaz et al., 2007). We then normalized the coefficients by dividing by the maximum coefficient value. Finally, we multiplied the absolute value of normalized coefficients by the base classifier's weight of voting as feature weights. The higher the feature weights were determined to be, the more discriminative of corresponding features. On every fold of LOOCV, the selected features differed slightly from fold to fold of LOOCV. The most discriminative features were restricted to those that appeared in every fold of LOOCV. Each base classifier's feature weights were averages from all folds of LOOCV. The feature weights of the multi-classifier were finally obtained by summing the base classifier's feature weights. Thus, for 90 ROIs, we obtained the order of their contribution to the classification.

The matlab codes relevant to the M3 method have been made publicly available at: <http://www.nitrc.org/projects/pare/>.

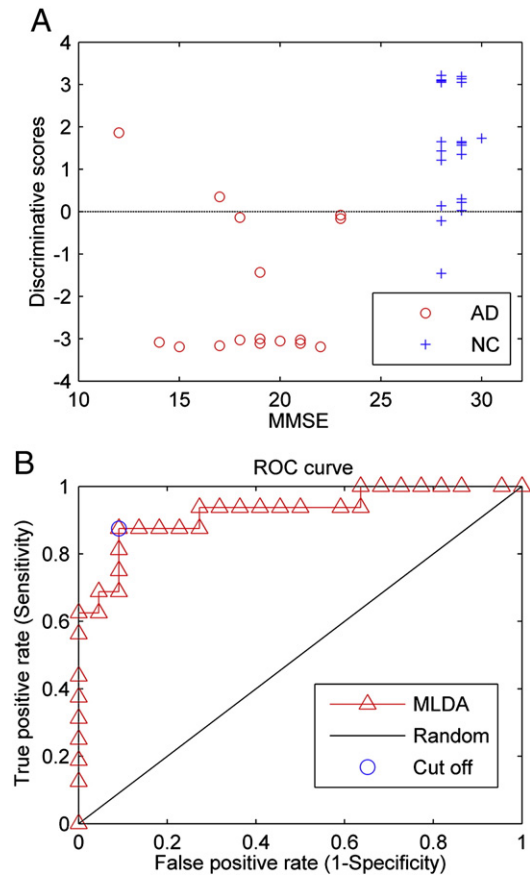


**Fig. 2.** Classification performance of the M3 method. (A) Scatter plot of the discriminative scores of all subjects in the multi-classifier. Negative scores represent subjects classified in the AD group and positive scores represent subjects classified in the healthy control group. (B) ROC curve of the classifier. The cut-off point corresponds to the highest accuracy of 89.47%. The area under the ROC curve was 0.923.

## Results

We used a LOOCV to estimate the generalizability of the classifier. Our M3 method achieved a classification accuracy of 89.47%, with a sensitivity of 87.5% and a specificity of 90.91%. These results were better than the values obtained with any single type of feature or other types of multi-type features combinations. The classification performance of the combined and simple types of features is summarized in Table 3. We also listed the number of features retained in the M3 method per fold in Table 4.

Fig. 2A presents the relationship between discriminative scores and MMSE. The discriminative score for each test subject acquired by the multi-classifier was determined by weighted voting by the four base classifiers. Taking each subject's discriminative score as a threshold, the performance in terms of the receiver operating characteristics (ROC) curve is shown in Fig. 2B. The area under the ROC curve (AUC) of the proposed method was 0.923, indicating an excellent diagnostic power.

The most discriminative features for classification are shown in Table 5 and Fig. 3. The top 15 features are listed in descending order of their weights. The ROIs with the great relative classification power included the bilateral fusiform gyrus (FFG), the right medial orbital of superior frontal gyrus (ORBsupmed), bilateral hippocampus (HIP), the right inferior occipital gyrus (IOG), the left middle occipital gyrus (MOG), bilateral amygdala (AMYG), the left posterior cingulate gyrus (PCG), the right orbital part of superior frontal gyrus (ORBsup), the left pallidum of the lenticular nucleus (PAL), the right parahippocampal gyrus (PHG), the right insula (INS) and the left Heschl gyrus (HES). We also listed whether these features demonstrated significant differences in each type of feature. Compared with the healthy controls, the AD patients showed significant ALFF increases in the bilateral FFG, the right ORBsupmed and left the HIP, ReHo increases in the bilateral FFG and RFCS increases in the left MOG, while AD

patients showed significant ALFF decreases in the left PCG, ReHo decreases in the right ORBsupmed, right ORBsup and left PAL and RFCS decreases in the right ORBsupmed and right INS and GMD decreases in all these ROIs except left PAL.

## Discussion

In the present study, we introduced the M3 method, which can be used to discriminate AD patients from healthy controls. A promising classification performance has been validated with LOOCV: our method achieved a high accuracy (89.47%) for AD classification, and the AUC value of the proposed method was 0.923. In addition, our M3 method can substantially improve the classification performance, especially the sensitivity rate, compared with the individual modality base classifier and other multi-modal multi-level combination classification. Thus, this method is more effective in conveying comprehensive and complementary information for the purpose of classification. It is worth noting that the classification performance is not always improved when more features are used (Fan et al., 2007).

The proposed approach seeks to identify features that discriminate the most between AD and healthy controls. These features included the FFG, ORBsupmed, HIP, IOG, MOG, AMYG, PCG, ORBsup, PAL, PHG, INS and HES, which are consistent with previous studies that have used conventional univariate statistical analysis of structural and functional images to classify AD. VBM studies showed that all of these regions had significant atrophy in AD patients compared to healthy controls (Baron et al., 2001; Chetelat and Baron, 2003). ALFF studies found increased ALFF values in the FFG and HIP and decreased ALFF values in the PCG in AD patients (Wang et al., 2011). ReHo studies reported significant ReHo increases in the FFG in AD patients (He et al., 2007). Whole brain network functional connectivity analysis indicated that AD patients had decreased positive correlations between

**Table 5**

Top 15 features showing the most discriminative features for classification.

Regions	ALFF	ReHo	RFCS	GMD	Weight
Right fusiform	t = 3.40 (P = 0.0017)	t = 3.05 (P = 0.0043)	NS	t = -6.76 (P < 0.0001)	1.574
Right superior frontal gyrus, medial orbital	t = 2.26 (P = 0.0301)	t = -2.73 (P = 0.0098)	t = -3.29 (P = 0.0023)	t = -5.16 (P < 0.0001)	1.360
Left fusiform	t = 4.59 (P < 0.0001)	t = 2.18 (P = 0.036)	NS	t = -6.51 (P < 0.0001)	1.019
Left hippocampus	t = 2.83 (P = 0.0076)	NS	NS	t = -7.39 (P < 0.0001)	0.974
Right hippocampus	NS	NS	NS	t = -7.66 (P < 0.0001)	0.865
Right inferior occipital gyrus	NS	NS	NS	t = -7.07 (P < 0.0001)	0.857
Left middle occipital gyrus	NS	NS	t = 3.53 (P = 0.0012)	t = -5.44 (P < 0.0001)	0.855
Right amygdala	NS	NS	NS	t = -6.28 (P < 0.0001)	0.774
Left posterior cingulate gyrus	t = -4.38 (P < 0.0001)	NS	NS	t = -5.45 (P < 0.0001)	0.761
Right superior frontal gyrus, orbital part	NS	t = -3.56 (P = 0.0011)	NS	t = -4.97 (P < 0.0001)	0.750
Left lenticular nucleus, pallidum	NS	t = -4.29 (P = 0.0001)	NS	NS	0.739
Right parahippocampal gyrus	NS	NS	NS	t = -7.14 (P < 0.0001)	0.701
Left amygdala	NS	NS	NS	t = -6.55 (P < 0.0001)	0.664
Right insula	NS	NS	t = -2.95 (P = 0.0055)	t = -6.52 (P < 0.0001)	0.653
Left heschl	NS	NS	NS	t = -6.51 (P < 0.0001)	0.624

NS:  $P > 0.05$ , uncorrected.

Positive t value means increased values in the AD group.

Regions were ranked according to the feature weights.

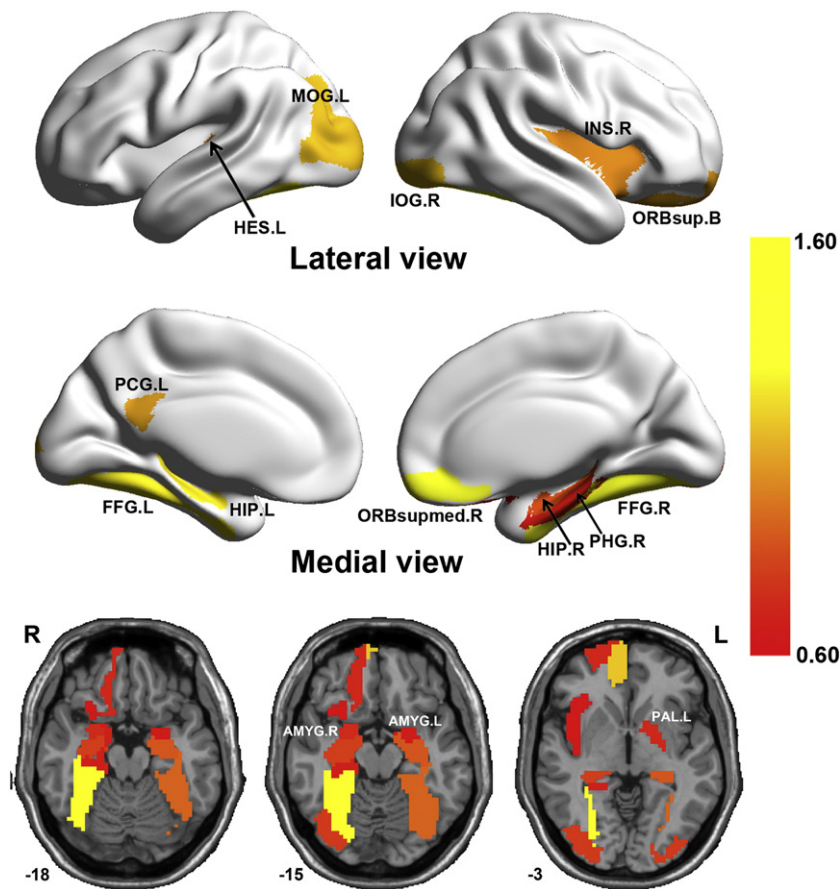


**Fig. 3.** The brain regions with the most discrimination power. To visually represent the relative contribution of brain regions for classification, the ROIs were projected onto a human brain atlas. The color represents the feature weight for each ROI. The 3D maps were made by using the BrainNet Viewer (<http://www.nitrc.org/projects/bnv/>). Several subcortical regions (bilateral AMYG and left PAL) are shown in 2D slice images. (For interpretation of the references to color in this figure legend, the reader is referred to the web version of this article.)

the prefrontal and parietal lobes (Wang et al., 2007). Our experimental results are consistent with these previous studies.

In conventional classification methods, the features were usually concatenated into a longer feature vector. However, these methods may not be sufficiently effective for combining features from different modalities (Zhang et al., 2011). Hence, we also tested direct feature concatenation for classification. Specifically, for each subject, we first concatenated 90 features from ALFF, 90 features from ReHo, 90 features from RFCS and 90 features from GMD into a 360 dimensional vector. We then performed feature selection and MLDA-based classification as described above on all of the subjects with LOOCV. The classification accuracy was 73.68%, which was lower than the accuracy achieved with our method. In this paper, we employed a multi-classifier to integrate different biomarkers. Compared with the direct feature concatenation method, the proposed method has the advantage of offering more flexibility by using different weights on different modalities. This method may provide us with a better way to combine different types of features for classification.

In addition to the feature combination, the base classifier is an important aspect of classification. Although more complex nonlinear classifiers exist, linear classifiers were used in the current study because they are less sensitive to overfitting. In addition, linear classifiers allow us to intuitively identify the most discriminative features by the projective direction. There are currently multiple linear classifiers available, including the FDA, linear support vector machine (SVM) and MLDA, all of which have been previously applied for neuroimaging data analysis (De Martino et al., 2008; Kloppel et al., 2008; Robinson et al., 2010; Thomaz et al., 2007; Wang et al., 2006; Zhu et al., 2008). Compared with FDA, MLDA can solve the problem that

within-class scatter matrix is singular in the case of limited samples and high dimensional feature space. Further analysis revealed higher generation rate of MLDA-based multi-classifier (89.47%) in comparison with linear SVM-based multi-classifier (81.58%) for our data set. Several previous studies have also found similar results in which SVM did not outperform LDA (Yang, 2001; Zhu et al., 2008). The theoretical comparison between MLDA and the linear SVM is not easy because they have different objective classification functions. MLDA seeks out the optimal projective direction by maximizing between-class separability and minimizing within-class variability, whereas linear SVM finds the solution to maximize (Zhu et al., 2008).

Several issues need to be addressed. First, we used a relatively low sampling rate ( $TR=2$  s) for imaging acquisitions. Under this sampling rate, cardiac and respiratory fluctuation effects were aliased into the low-frequency fluctuations, which could reduce the specificity of the connectivity effect (Lowe et al., 1998; Teichert et al., 2010). Recent research has demonstrated that global signal is associated with respiration-induced fMRI signal (Birn et al., 2006; Chang and Glover, 2009). In the preprocessing analysis of functional connectivity, we therefore regressed out this global signal to reduce the effects of the respiration. Moreover, we used a temporal filtering (0.01–0.1 Hz) procedure to further reduce the effects of low-frequency drifts and high-frequency physiological noise. In the future, these physiological effects can be estimated and removed by simultaneously recording the respiratory and cardiac cycle during the data acquisition. Second, although we used both structural MRI and resting fMRI data, there are also other data modalities (e.g., PET, EEG and CSF) that can be used to further improve the classification performance. Third, we used the AAL atlas to parcellate the brain into 90 ROIs.

Currently, there are different structurally (Collins et al., 1995; Makris et al., 1999) and functionally (Benjaminsson, 2010; Craddock et al., 2011; De Luca et al., 2006; Dosenbach et al., 2010) defined brain atlases: different parcellation schemes could generate different results. Several recent studies have demonstrated that the connectivity patterns of brain networks can be affected by different parcellation atlases (Craddock et al., 2011; Wang et al., 2009; Zalesky et al., 2010). To evaluate the effects of the brain parcellation methods on classification performance, further studies are needed to apply our method to other brain atlases, even to a voxel level. These studies will be important to determine which parcellation strategy is the most sensitive to specific disease condition. Fourth, although the M3 method obtained a good performance from LOOCV, we must acknowledge that the contradiction between learning precision and generalization is almost unavoidable for the limited size of subjects and high-dimensional feature space. In pattern classification, a complex model could predict the training data but fail drastically on unseen data because of lacking of the generalization. Thus, the overfitting issue generally occurs for these models. In this study, we indeed used a complex double-loop feature selection to reduce dimensionality of features, which could lead to the overfitting. However, it needs to note that the feature selection procedure was carried out on the training sample only. Moreover, we employed a linear learning algorithm to classify the patients, which is insensitive to overfitting problems as compared to nonlinear learning algorithms. Further, a leave-one out cross-validation was used to evaluate the generalization of our method for new individuals, which reduced the artifact of over-training (Pereira et al., 2009). Fifth, considering that a small sample (38 subjects in total) was used in this study, the obtained classifier was specific to the current dataset and could not be general enough. In the future, we expect to apply the M3 method to a large AD dataset (e.g., ADNI2) to train a robust classifier and to check its generalization ability. Finally, this study did not include the patients with other forms of dementia such as fronto-temporal dementia and Lewy-body dementia. In the future, the proposed M3 method can be further used to discriminate the AD patients from patients with other dementia.

## Conclusion

In this study, we introduced the M3 method to discriminate patients with AD from healthy controls by combining multi-modal imaging and multi-level measures including the degree of regional activity, the degree of regional synchronization, the degree of global synchronization of spontaneous neuronal activity and regional gray matter density. The predictive power of this method was very high, yielding 89.47% accuracy. Moreover, the M3 method offered more flexibility by using different weights for different measures. This promising classification power suggests that this method may provide a complementary approach for potentially improving the clinical diagnosis of AD as well as other brain disorders.

## Acknowledgments

This work was supported by the Natural Science Foundation of China (Grant Nos. 81030028, 30870667 and 81000606), Beijing Natural Science Foundation (Grant No. 7102090) and the Scientific Research Foundation for the Returned Overseas Chinese Scholars (State Education Ministry, YH).

## References

- Allen, G., Barnard, H., McColl, R., Hester, A.L., Fields, J.A., Weiner, M.F., Ringe, W.K., Lipton, A.M., Brooker, M., McDonald, E., Rubin, C.D., Cullum, C.M., 2007. Reduced hippocampal functional connectivity in Alzheimer disease. *Arch. Neurol.* 64, 1482–1487.
- Apostolova, L.G., Hwang, K.S., Andrawis, J.P., Green, A.E., Babakhanian, S., Morra, J.H., Cummings, J.L., Toga, A.W., Trojanowski, J.Q., Shaw, L.M., Jack Jr., C.R., Petersen, R.C., Aisen, P.S., Jagust, W.J., Koeppe, R.A., Mathis, C.A., Weiner, M.W., Thompson, P.M., 2010. 3D PIB and CSF biomarker associations with hippocampal atrophy in ADNI subjects. *Neurobiol. Aging* 31, 1284–1303.
- Ashburner, J., Friston, K.J., 2005. Unified segmentation. *NeuroImage* 26, 839–851.
- Baron, J.C., Chételat, G., Desgranges, B., Percey, G., Landeau, B., de la Sayette, V., Eustache, F., 2001. In vivo mapping of gray matter loss with voxel-based morphometry in mild Alzheimer's disease. *NeuroImage* 14, 298–309.
- Benjaminsson, S., Fransson, P., Lansner, A., 2010. A novel model-free data analysis technique based on clustering in a mutual information space: application to resting-state fMRI. *Front. Syst. Neurosci.* 4, 13.
- Bennys, K., Rondouin, G., Vergnes, C., Touchon, J., 2001. Diagnostic value of quantitative EEG in Alzheimer's disease. *Neurophysiol. Clin. (Clinical Neurophysiology)* 31, 153–160.
- Besthorn, C., Zerfass, R., Geiger-Kabisch, C., Sattel, H., Daniel, S., Schreiter-Gasser, U., Förstl, H., 1997. Discrimination of Alzheimer's disease and normal aging by EEG data. *Electroencephalogr. Clin. Neurophysiol.* 103, 241–248.
- Birn, R.M., Diamond, J.B., Smith, M.A., Bandettini, P.A., 2006. Separating respiratory-variation-related fluctuations from neuronal-activity-related fluctuations in fMRI. *NeuroImage* 31, 1536–1548.
- Biswal, B., Zerrin Yetkin, F., Haughton, V.M., Hyde, J.S., 1995. Functional connectivity in the motor cortex of resting human brain using echo-planar MRI. *Magn. Reson. Med.* 34, 537–541.
- Biswal, B.B., Mennes, M., Zuo, X.N., Gohel, S., Kelly, C., Smith, S.M., Beckmann, C.F., Adelstein, J.S., Buckner, R.L., Colcombe, S., Dogonowski, A.M., Ernst, M., Fair, D., Hampson, M., Hoptman, M.J., Hyde, J.S., Kiviniemi, V.J., Kottler, R., Li, S.J., Lin, C.P., Lowe, M.J., Mackay, C., Madden, D.J., Madsen, K.H., Margulies, D.S., Mayberg, H.S., McMahon, K., Monk, C.S., Mostofsky, S.H., Nagel, B.J., Pekar, J.J., Peltier, S.J., Petersen, S.E., Riedel, V., Rombouts, S.A.R.B., Rypma, B., Schlaggar, B.L., Schmidt, S., Seidler, R.D., Siegle, G.J., Sorg, C., Teng, G.J., Vejjola, J., Villringer, A., Walter, M., Wang, L., Weng, X.C., Whitfield-Gabrieli, S., Williamson, P., Windischberger, C., Zang, Y.F., Zhang, H.Y., Castellanos, F.X., Milham, M.P., 2010. Toward discovery science of human brain function. *Proc. Natl. Acad. Sci.* 107, 4734–4739.
- Chang, C., Glover, G.H., 2009. Effects of model-based physiological noise correction on default mode network anti-correlations and correlations. *NeuroImage* 47, 1448–1459.
- Chapman, R.M., Nowlis, G.H., McCrary, J.W., Chapman, J.A., Sandoval, T.C., Guillily, M.D., Gardner, M.N., Reilly, L.A., 2007. Brain event-related potentials: diagnosing early-stage Alzheimer's disease. *Neurobiol. Aging* 28, 194–201.
- Chen, G., Ward, B.D., Xie, C., Li, W., Wu, Z., Jones, J.L., Franczak, M., Antuono, P., Li, S.J., 2011. Classification of Alzheimer disease, mild cognitive impairment, and normal cognitive status with large-scale network analysis based on resting-state functional MR imaging. *Radiology* 259, 213–221.
- Chételat, G., Baron, J.-C., 2003. Early diagnosis of Alzheimer's disease: contribution of structural neuroimaging. *NeuroImage* 18, 525–541.
- Collignon, A., Maes, F., Delaere, D., Vandermeulen, D., Suetens, P., Marchal, G., 1995. Automated multi-modality image registration based on information theory. *Inf. Process. Med. Imaging* 263–274.
- Collins, L., Holmes, C.J., Peters, T.M., Evans, A.C., 1995. Automatic 3-D model-based neuroanatomical segmentation. *Hum. Brain Mapp.* 3, 190–208.
- Craddock, R.C., James, G.A., Holtzheimer, P.E., Hu, X.P., Mayberg, H.S., 2011. A whole brain fMRI atlas generated via spatially constrained spectral clustering. *Hum. Brain Mapp.* doi:10.1002/hbm.21333.
- Davatzikos, C., Fan, Y., Wu, X., Shen, D., Resnick, S.M., 2008a. Detection of prodromal Alzheimer's disease via pattern classification of magnetic resonance imaging. *Neurobiol. Aging* 29, 514–523.
- Davatzikos, C., Resnick, S.M., Wu, X., Parmpi, P., Clark, C.M., 2008b. Individual patient diagnosis of AD and FTD via high-dimensional pattern classification of MRI. *NeuroImage* 41, 1220–1227.
- De Luca, M., Beckmann, C.F., De Stefano, N., Matthews, P.M., Smith, S.M., 2006. fMRI resting state networks define distinct modes of long-distance interactions in the human brain. *NeuroImage* 29, 1359–1367.
- De Martino, F., Valente, G., Staeren, N., Ashburner, J., Goebel, R., Formisano, E., 2008. Combining multivariate voxel selection and support vector machines for mapping and classification of fMRI spatial patterns. *NeuroImage* 43, 44–58.
- Desikan, R.S., Cabral, H.J., Hess, C.P., Dillon, W.P., Glastonbury, C.M., Weiner, M.W., Schmansky, N.J., Greve, D.N., Salat, D.H., Buckner, R.L., Fischl, B., 2009. Automated MRI measures identify individuals with mild cognitive impairment and Alzheimer's disease. *Brain* 132, 2048–2057.
- Dosenbach, N.U.F., Nardos, B., Cohen, A.L., Fair, D.A., Power, J.D., Church, J.A., Nelson, S.M., Wig, G.S., Vogel, A.C., Lessov-Schlaggar, C.N., Barnes, K.A., Dubis, J.W., Feczko, E., Coalson, R.S., Pruett, J.R., Barch, D.M., Petersen, S.E., Schlaggar, B.L., 2010. Prediction of individual brain maturity using fMRI. *Science* 329, 1358–1361.
- Fan, Y., Rao, H., Hurt, H., Giannetta, J., Korczykowski, M., Shera, D., Avants, B.B., Gee, J.C., Wang, J., Shen, D., 2007. Multivariate examination of brain abnormality using both structural and functional MRI. *NeuroImage* 36, 1189–1199.
- Fox, M.D., Greicius, M., 2010. Clinical applications of resting state functional connectivity. *Front. Syst. Neurosci.* 4, 19.
- Fox, M.D., Raichle, M.E., 2007. Spontaneous fluctuations in brain activity observed with functional magnetic resonance imaging. *Nat. Rev. Neurosci.* 8, 700–711.
- Fox, M.D., Snyder, A.Z., Vincent, J.L., Corbetta, M., Van Essen, D.C., Raichle, M.E., 2005. The human brain is intrinsically organized into dynamic, anticorrelated functional networks. *Proc. Natl. Acad. Sci. U. S. A.* 102, 9673–9678.
- Greicius, M.D., Srivastava, G., Reiss, A.L., Menon, V., 2004. Default-mode network activity distinguishes Alzheimer's disease from healthy aging: evidence from functional MRI. *Proc. Natl. Acad. Sci. U. S. A.* 101, 4637–4642.
- Guyon, I., 2003. An introduction to variable and feature selection. *J. Mach. Learn. Res.* 3, 1157–1182.

- He, Y., Wang, L., Zang, Y., Tian, L., Zhang, X., Li, K., Jiang, T., 2007. Regional coherence changes in the early stages of Alzheimer's disease: a combined structural and resting-state functional MRI study. *NeuroImage* 35, 488–500.
- He, Y., Dagher, A., Chen, Z., Charil, A., Zijdenbos, A., Worsley, K., Evans, A., 2009. Impaired small-world efficiency in structural cortical networks in multiple sclerosis associated with white matter lesion load. *Brain* 132, 3366–3379.
- Hirata, Y., Matsuda, H., Nemoto, K., Ohnishi, T., Hirao, K., Yamashita, F., Asada, T., Iwabuchi, S., Samejima, H., 2005. Voxel-based morphometry to discriminate early Alzheimer's disease from controls. *Neurosci. Lett.* 382, 269–274.
- Hong, L., Jain, A., Pankanti, S., 1999. Can multibiometrics improve performance. *Proc. AUTOID*.
- Jeong, J., 2004. EEG dynamics in patients with Alzheimer's disease. *Clin. Neurophysiol.* 115, 1490–1505.
- Jiang, T., He, Y., Zang, Y., Weng, X., 2004. Modulation of functional connectivity during the resting state and the motor task. *Hum. Brain Mapp.* 22, 63–71.
- Karas, G.B., Burton, E.J., Rombouts, S.A.R.B., van Schijndel, R.A., O'Brien, J.T., Scheltens, P., McKeith, I.G., Williams, D., Ballard, C., Barkhof, F., 2003. A comprehensive study of gray matter loss in patients with Alzheimer's disease using optimized voxel-based morphometry. *NeuroImage* 18, 895–907.
- Kendall, M.G., Gibbons, J.D., 1990. Rank correlation methods. E. Arnold; Oxford University Press, London; New York, NY.
- Kippenhan, J.S., Barker, W.W., Nagel, J., Grady, C., Duara, R., 1994. Neural-network classification of normal and Alzheimer's disease subjects using high-resolution and low-resolution PET cameras. *J. Nucl. Med.* 35, 7–15.
- Kittler, J., Hatef, M., Duin, R.P.W., Matas, J., 1998. On combining classifiers. *IEEE Trans. Pattern Anal. Mach. Intell.* 20, 226–239.
- Kloppel, S., Stonnington, C.M., Chu, C., Draganski, B., Scahill, R.I., Rohrer, J.D., Fox, N.C., Jack, C.R., Ashburner, J., Frackowiak, R.S.J., 2008. Automatic classification of MR scans in Alzheimer's disease. *Brain* 131, 681–689.
- Lao, Z., Shen, D., Xue, Z., Karacali, B., Resnick, S.M., Davatzikos, C., 2004. Morphological classification of brains via high-dimensional shape transformations and machine learning methods. *NeuroImage* 21, 46–57.
- Lee, D.Y., Lee, J.H., Ju, Y.-S., Kang Uk Lee, M.D., Kim, K.W., Jhoo, J.H., Yoon, J.C., Ha, J., Woo, J.I., 2002. The prevalence of dementia in older people in an urban population of Korea: the Seoul study. *J. Am. Geriatr. Soc.* 50, 1233–1239.
- Lehmann, C., Koenig, T., Jelic, V., Prichep, L., John, R.E., Wahlund, L.-O., Dodge, Y., Dierks, T., 2007. Application and comparison of classification algorithms for recognition of Alzheimer's disease in electrical brain activity (EEG). *J. Neurosci. Methods* 161, 342–350.
- Lerch, J.P., Pruessner, J., Zijdenbos, A.P., Collins, D.L., Teipel, S.J., Hampel, H., Evans, A.C., 2008. Automated cortical thickness measurements from MRI can accurately separate Alzheimer's patients from normal elderly controls. *Neurobiol. Aging* 29, 23–30.
- Li, S.-J., Li, Z., Wu, G., Zhang, M.-J., Franczak, M., Antuono, P.G., 2002. Alzheimer disease: evaluation of a functional MR imaging index as a Marker1. *Radiology* 225, 253–259.
- Lowe, M.J., Mock, B.J., Sorenson, J.A., 1998. Functional connectivity in single and multi-slice echoplanar imaging using resting-state fluctuations. *NeuroImage* 7, 119–132.
- Magnin, B., Mesrob, L., Kinkingnéhun, S., Péligrini-Issac, M., Colliot, O., Sarazin, M., Dubois, B., LeHérecy, S., Benali, H., 2008. Support vector machine-based classification of Alzheimer's disease from whole-brain anatomical MRI. *Neuroradiology* 51, 73–83.
- Makris, N., Meyer, J.W., Bates, J.F., Yeterian, E.H., Kennedy, D.N., Caviness Jr., V.S., 1999. MRI-based topographic parcellation of human cerebral white matter and nuclei: II. Rationale and applications with systematics of cerebral connectivity. *NeuroImage* 9, 18–45.
- McKhann, G., Drachman, D., Folstein, M., Katzman, R., Price, D., Stadlan, E.M., 1984. Clinical diagnosis of Alzheimer's disease. *Neurology* 34, 939.
- Minoshima, S., Frey, K.A., Koeppe, R.A., Foster, N.L., Kuhl, D.E., 1995. A diagnostic approach in Alzheimer's disease using three-dimensional stereotactic surface projections of fluorine-18-FDG PET. *J. Nucl. Med.* 36, 1238–1248.
- Morris, J.C., 1993. The Clinical Dementia Rating (CDR): current version and scoring rules. *Neurology* 43, 2412–2414.
- Mourão-Miranda, J., Bokde, A.L.W., Born, C., Hampel, H., Stetter, M., 2005. Classifying brain states and determining the discriminating activation patterns: support vector machine on functional MRI data. *NeuroImage* 28, 980–995.
- Pereira, F., Mitchell, T., Botvinick, M., 2009. Machine learning classifiers and fMRI: a tutorial overview. *NeuroImage* 45, S199–S209.
- Robinson, E.C., Hammers, A., Ericsson, A., Edwards, A.D., Rueckert, D., 2010. Identifying population differences in whole-brain structural networks: a machine learning approach. *NeuroImage* 50, 910–919.
- Ross, A., Jain, A., 2003. Information fusion in biometrics. *Pattern Recognit. Lett.* 24, 2115–2125.
- Sato, J.R., Fujita, A., Thomaz, C.E., Martin, M.G.M., Mourão-Miranda, J., Brammer, M.J., Junior, E.A., 2009. Evaluating SVM and MLDA in the extraction of discriminant regions for mental state prediction. *NeuroImage* 46, 105–114.
- Song, X.W., Dong, Z.Y., Long, X.Y., Li, S.F., Zuo, X.N., Zhu, C.Z., He, Y., Yan, C.G., Zang, Y.F., 2011. REST: A Toolkit for Resting-State Functional Magnetic Resonance Imaging Data Processing. *PLoS One* 6, e25031.
- Supekar, K., Menon, V., Rubin, D., Musen, M., Greicius, M.D., 2008. Network analysis of intrinsic functional brain connectivity in Alzheimer's disease. *PLoS Comput. Biol.* 4, e1000100.
- Talairach, J., Tournoux, P., 1988. Co-planar stereotaxic atlas of the human brain. Thieme Medical, New York.
- Teichert, T., Grinband, J., Hirsch, J., Ferrera, V.P., 2010. Effects of heartbeat and respiration on macaque fMRI: Implications for functional connectivity. *Neuropsychologia* 48, 1886–1894.
- Thomaz, C.E., Boardman, J.P., Hill, D.L.G., Hajnal, J.V., Edwards, A.D., Rutherford, M.A., Gillies, D.F., Rueckert, D., 2004. Whole brain voxel-based analysis using registration and multivariate statistics. Proceedings of the 8th Medical Image Understanding and Analysis MIUA'04. BMVA Press, London, UK, pp. 73–76.
- Thomaz, C., Boardman, J., Counsell, S., Hill, D., Hajnal, J., Edwards, A., Rutherford, M., Gillies, D., Rueckert, D., 2007. A multivariate statistical analysis of the developing human brain in preterm infants. *Image Vision Comput.* 25, 981–994.
- Tzourio-Mazoyer, N., 2002. Automated anatomical labeling of activations in SPM Using a macroscopic anatomical parcellation of the MNI MRI single-subject brain. *NeuroImage* 15, 273–289.
- Walhovd, K.B., Fjell, A.M., Brewer, J., McEvoy, L.K., Fennema-Notestine, C., Hagler, D.J., Jennings, R.G., Karow, D., Dale, A.M., 2010. Combining MR imaging, positron-emission tomography, and CSF biomarkers in the diagnosis and prognosis of Alzheimer disease. *Am. J. Neuroradiol.* 31, 347–354.
- Wang, K., Jiang, T., Liang, M., Wang, L., Tian, L., Zhang, X., Li, K., Liu, Z., 2006. Discriminative analysis of early Alzheimer's disease based on two intrinsically anti-correlated networks with resting-state fMRI. *Med. Image Comput. Comput. Assist. Interv.* 9, 340–347.
- Wang, K., Liang, M., Wang, L., Tian, L., Zhang, X., Li, K., Jiang, T., 2007. Altered functional connectivity in early Alzheimer's disease: a resting-state fMRI study. *Hum. Brain Mapp.* 28, 967–978.
- Wang, J., Wang, L., Zang, Y., Yang, H., Tang, H., Gong, Q., Chen, Z., Zhu, C., He, Y., 2009. Parcellation-dependent small-world brain functional networks: a resting-state fMRI study. *Hum. Brain Mapp.* 30, 1511–1523.
- Wang, J., Zuo, X., He, Y., 2010. Graph-based network analysis of resting-state functional MRI. *Front Syst Neurosci* 4, 16.
- Wang, Z., Yan, C., Zhao, C., Qi, Z., Zhou, W., Lu, J., He, Y., Li, K., 2011. Spatial patterns of intrinsic brain activity in mild cognitive impairment and Alzheimer's disease: A resting-state functional MRI study. *Hum. Brain Mapp.* 32, 1720–1740.
- Yan, C.G., Zang, Y.F., 2010. DPARSF: a MATLAB toolbox for "Pipeline" data analysis of resting-state fMRI. *Front. Syst. Neurosci.* 4, 13.
- Yang, M., 2001. Face detection using multimodal density models. *Comput. Vision Image Understanding* 84, 264–284.
- Zalesky, A., Fornito, A., Harding, I.H., Cocchi, L., Yücel, M., Pantelis, C., Bullmore, E.T., 2010. Whole-brain anatomical networks: does the choice of nodes matter? *NeuroImage* 50, 970–983.
- Zang, Y., Jiang, T., Lu, Y., He, Y., Tian, L., 2004. Regional homogeneity approach to fMRI data analysis. *NeuroImage* 22, 394–400.
- Zang, Y., Yong, H., Chaozhe, Z., Qingjiu, C., Manqiu, S., Meng, L., Lixia, T., Tianji, J., Yufeng, W., 2007. Altered baseline brain activity in children with ADHD revealed by resting-state functional MRI. *Brain Dev.* 29, 83–91.
- Zhang, D., Raichle, M.E., 2010. Disease and the brain's dark energy. *Nat. Rev. Neurol.* 6, 15–28.
- Zhang, D., Wang, Y., Zhou, L., Yuan, H., Shen, D., 2011. Multimodal classification of Alzheimer's disease and mild cognitive impairment. *NeuroImage* 55, 856–867.
- Zhu, C.-Z., Zang, Y.-F., Cao, Q.-J., Yan, C.-G., He, Y., Jiang, T.-Z., Sui, M.-Q., Wang, Y.-F., 2008. Fisher discriminative analysis of resting-state brain function for attention-deficit/hyperactivity disorder. *NeuroImage* 40, 110–120.